# Experimental investigation of convective heat transfer for night cooling with diffuse ceiling ventilation

Guo, Rui; Heiselberg, Per; Hu, Yue; Johra, Hicham; Zhang, Chen; Jensen, Rasmus Lund; Jønsson, Kim Trangbæk; Peng, Pei

*Published in:*
Building and Environment

*DOI (link to publication from Publisher):*
10.1016/j.buildenv.2021.107665



*Publication date:*
2021

*Document Version*
Accepted author manuscript, peer reviewed version

# Experimental investigation of heat transfer for night cooling with diffuse ceiling ventilation

Rui Guo*, Per Heiselberg, Yue Hu, Hicham Johra, Chen Zhang, Rasmus Lund Jensen, Kim Trangbæk Jønsson, Pei Peng

*Department of the Built Environment, Aalborg University, Thomas Manns Vej 23, Aalborg 9220, Denmark*

**Corresponding author email address: rgu@build.aau.dk*

## ABSTRACT

The convective heat transfer coefficient (CHTC) is a crucial parameter for night ventilation performance estimation. This paper investigates the heat transfer of night ventilation with diffuse ceiling ventilation (DCV) concept in an office room. A series of dynamic full-scale experiments were conducted with different thermal mass distribution schemes, air change rates per hour (ACH), and supply temperatures. The CHTC at interior surfaces with the inlet and outlet temperatures as the reference and the temperature efficiency of DCV were then derived. In most cases, the experimental CHTCs differed significantly from the CHTCs predicted by existing correlations. The presence of furniture (tables), its location, and the thermal mass installed on the walls had little influence on the CHTC at the floor. However, increasing the thermal mass of one surface can significantly augment its own surface CHTC. New correlations based on experimental CHTCs were developed for potential application in building energy simulation tools. The temperature efficiency of DCV decreased with the increase of ACH, the initial temperature difference between the supply air and indoor air, and the thermal mass level. DCV had higher temperature efficiency than the mixing ventilation and displacement ventilation, except for the case with displacement ventilation at low ACH.

## KEYWORDS

Convective heat transfer coefficient; Night ventilation; Diffuse ceiling ventilation; Dynamic full-scale experiments.

## Nomenclature

*Latin symbols*

| | |
|---|---|
| $A$ | Area |
| $c$ | Heat capacity |
| $C$ | Constant |
| $C_{\mathrm{P}}$ | Specific heat capacity |
| $E_{\mathrm{b}}$ | Black body emissive power |
| $F$ | View factor |
| $g$ | Gravitational acceleration |
| $h$ | Surface heat transfer coefficient |
| $H$ | Height of walls |
| $k$ | Air thermal conductivity |
| $L$ | Characteristic length |
| $\dot{m}$ | Air volume flow rate |
| $q$ | Heat flux |
| $Q$ | Heat flow |
| $T$ | Temperature |
| $u$ | Airflow speed |

*Greek symbols*

| | |
|---|---|
| $\Delta$ | Change in a variable |
| $\delta$ | Kronecker symbol |
| $\varepsilon$ | Emissivity |
| $\rho$ | Density |
| $v$ | Air dynamic viscosity |
| $\lambda$ | Thermal conductivity |

*Subscript*

| | |
|---|---|
| *conv* | Convective |
| *cond* | Conductive |
| *rad* | Radiative |
| *surf* | Surface |
| *i*,*j* | Index for surface *i* and *j* |

*Acronyms*

| | |
|---|---|
| ACH | Air change rate per hour |
| AHU | Air handling unit |
| BES | Building energy simulation |
| CCP | Climatic cooling potential |
| CFD | Computational fluid dynamics |
| CHTC | Convective heat transfer coefficient |
| CTF | Conduction transfer function module |
| DCV | Diffuse ceiling ventilation |
| HAMT | Combined heat and moisture transfer module |
| LHS | Latin Hypercube Sampling |
| MCA | Monte Carlo analysis |
| NV | Night ventilation |
| Re | Reynolds number |
| Nu | Nusselt number |

# 1 INTRODUCTION

Night ventilation (NV) is a promising way to alleviate the overheating in buildings and reduce the building cooling demand by using cold outdoor air to cool down the building's thermal mass. The cooled thermal mass then acts as a heat sink on the next day to absorb the heat gain and stabilize the indoor air temperature [1]. During the daytime, the purpose of cooling methods is to maintain the indoor air temperature within the thermal comfort range, limiting the airflow rate and inlet temperature decrease to avoid draught. The purpose of NV is to purge out the diurnal excess heat stored in the thermal mass by convection when the office building is not occupied. The added benefit of NV is that the indoor air temperature limit of NV can be as low as 18 °C, and the air change rate per hour (ACH) can be high up to 10 $h^{-1}$ [2].

Although NV has the benefits mentioned above and has been investigated widely in experimental or simulation research [3–8], architects or engineers still hesitate to adopt this solution due to the high uncertainty in performance prediction caused by the inaccurate CHTC at interior surfaces. Several studies identified the convective heat transfer (CHTC) as a critical parameter necessary to predict the NV performance [9–11]. Numerous empirical CHTC correlations have been developed based on the steady flat plat or steady full-scale experiments [12] and widely adopted in building energy simulation (BES) tools [13]. Nevertheless, those correlations are only applicable to specific conditions (e.g., radial ceiling diffuser or displacement ventilation), which may not be adequate for NV and cause a large error in NV simulations. Previous studies [14–16] investigated the heat transfer of NV with mixing ventilation, displacement ventilation, and wall-mounted attached ventilation by dynamic full-scale experiments. However, those studies did not focus on characterizing CHTC or developing CHTC correlation.

Thermal mass activation also plays a decisive role in NV efficiency [17]. Goethals et al. simulated surrogate models based on CFD [18] and tested the conditions [19] in a modified

PASLINK cell (an outdoor climate chamber) to investigate the convective heat flux in a night cooled office room with different ventilation concepts, thermal mass distributions, and room geometries. The results showed that the thermal mass could augment the convective heat flux on the surface. Besides the thermal mass on the interior surfaces of buildings, a few studies investigated the impact of furniture (a kind of internal thermal mass) on the heat transfer in the room. Wallentén [20] conducted a full-scale experiment involving a desk, two chairs, and a small chest. The impact of furniture on the convective heat transfer was found to be small. Spitler et al. [21] indicated that the furniture (one table and six chairs/two cabinets) impacted the airflow by comparing the airflow of the room with and without furniture. Those studies focused more on the convective heat flux or airflow rather than analyzing the CHTC at surfaces.

Diffuse ceiling ventilation (DCV) is an air distribution concept originally developed for livestock buildings but attracting growing interest for buildings with human occupancy in recent years [22]. This air distribution system comprises three components: the air plenum, the suspended ceiling, and the ventilated room. The basic principle of DCV is to induce outdoor air or supply conditioned air to the plenum before air diffuses through the suspended ceiling panel into the occupied zone [23]. The plenum acts as the "air duct" to distribute the air; thus, reducing or replacing the common duct. The large suspended ceiling panel is characterized as an air diffuser that supplies the air to the occupied zone with very low velocity, which can utilize extremely low-temperature air without increasing the risk of draught. Furthermore, the pressure drop through the suspended ceiling panel is much lower than conventional diffusers and air ducts, saving fan energy use and providing natural ventilation potential [24]. Several studies have investigated the DCV performance in buildings concerning thermal comfort [25–28] and energy performance [29–32] by full-scale experiments or numerical simulations.

Taking account of the advantages mentioned above, DCV should also have a high night cooling potential. Indeed, the outdoor air is circulated throughout the building to effectively remove the

stored heat in building components, especially the ceiling slab in which the plenum is directly exposed to the ambient air [33]. However, only a few studies have investigated the night cooling potential using DCV. Hviid [34] simulated the local CHTC in the plenum by computational fluid dynamics (CFD) and input those values in BES to evaluate the night cooling potential. The simulated combined CHTC (i.e., convective + radiative) at the ceiling slab in the plenum was 11 $W/m^2 \cdot K$, only 1 $W/m^2 \cdot K$ higher than the prescribed value in the Danish standard for building heat transfer calculations [35]. NV with DVC significantly reduced the overheating hours and lowered the peak temperature. Hviid and Lessing [36] derived the total CHTC of the plenum by a full-scale experiment and used the results in a BES tool to simulate NV's cooling effect. Compared to the room without DCV, the total CHTC of the plenum was greatly increased, and the occupied zone temperature reduced 1 – 1.5 °C, which showed the free cooling potential by utilizing the thermal mass in the ceiling slab. Those studies focused on the heat transfer in the plenum rather than the ventilated room, which has a larger interior surface area that directly affects human thermal comfort and the energy use by absorbing the heat gain during the daytime.

Furthermore, few studies have modeled the building energy performance with DCV only. According to the authors' knowledge and literature review, only one thermally activated building system integrated with DCV was modeled in BES tools [31]. The results showed that unlike the surfaces in the plenum cooled day and night by conditioned air or cold ambient air, the surfaces in the ventilated room absorb internal and solar heat gains and impact human comfort by radiation directly. Zhang et al. [37] demonstrated that for DCV, the buoyancy flow from heat sources controls the room's airflow pattern when the ACH is not higher than 10 $h^{-1}$. NV usually drives a predominately forced convection heat flow because there is no heat source or solar irradiance in the office room at night [14]. The heat transfer of the ventilated room with DCV at night cooling scenario needs further study.

To the best of the authors' knowledge, this paper aims to analyze the CHTC at surfaces in a ventilated room and the temperature efficiency of DCV under the NV scenario. The study also investigates the impact of thermal mass distribution on the CHTC, compares the CHTC with existing correlations, and develops CHTC correlations. The dynamic full-scale experiments were conducted in 25 design cases involving 6 thermal mass distribution schemes, 3 constant ACH, and 2 supply air temperatures. Section 2 describes the experimental setup. Section 3 introduces the data analysis methods for the derivation of CHTC and uncertainty analysis. Section 4 presents the experimental CHTCs at surfaces of the ventilated room. Section 5 summarizes the conclusions and closes the article with suggestions for future work.

# 2 EXPERIMENTAL DESCRIPTIONS

## 2.1 Guarded hot box setup

The Standard EN ISO 8990 defines two types of hot box apparatuses: the guarded hot box and the calibrated hot box [38]. A guarded hot box was used as a test chamber to conduct the dynamic full-scale experiments (see Fig. 1). The hot box was divided into three zones: a guarding zone, an upper zone, and a test room. The upper zone was an air plenum that represents the space between the room ceiling and diffuse ceiling in a real building, while the test room represents the office room with dimensions of 4.2 m (L)×3.6 m (W)×2.5 m (H). The guarding zone enclosed the upper zone and test room with the constant air temperature (22 °C) by an air handling unit (AHU) to simulate a stable outdoor environment for ensuring that the heat loss of envelope was only caused by NV. The temperature of 22 °C is a representative temperature for the office building at the end of the summer working day [39]. Another AHU supplied the conditioned air into the upper zone and exhausted the air in the test room by a circular outlet with a diameter of 215 mm located in the bottom right corner of the front wall shown in Fig. 2a. A duct with an airflow sensor was connected to the outlet to measure the airflow rate. A fabric air duct with a diameter of 300 mm in the upper zone was applied to distribute the air in

the upper zone uniformly (see Fig. 2c). The diffuse ceiling panels made by wood-cement boards ($\rho$=359 kg/m$^3$, $C_p$=923 J/kg·K, $\lambda$=0.085 W/m·K, porosity = 65%) with a thickness of 25 mm separated the upper zone and test room (see Fig. 2d).

The original construction of three walls (right, back, and left) and floor in the test room was sandwich elements (i.e., 15 mm wood panel+225 mm expanded polystyrene+15 mm wood panel). The front wall comprised 150 mm foam boards ($\rho$=14.5 kg/m$^3$, $C_p$=1500 J/kg·K, $\lambda$=0.038 W/m·K) and 12 mm wood panels. The front wall was in contact with the indoor laboratory environment, conditioned at a constant temperature of 22 °C. To achieve better insulation, 50 mm foam boards were installed on the test room's interior surfaces. Due to the practical door open position in the room, 100 mm foam boards were installed on the back wall.

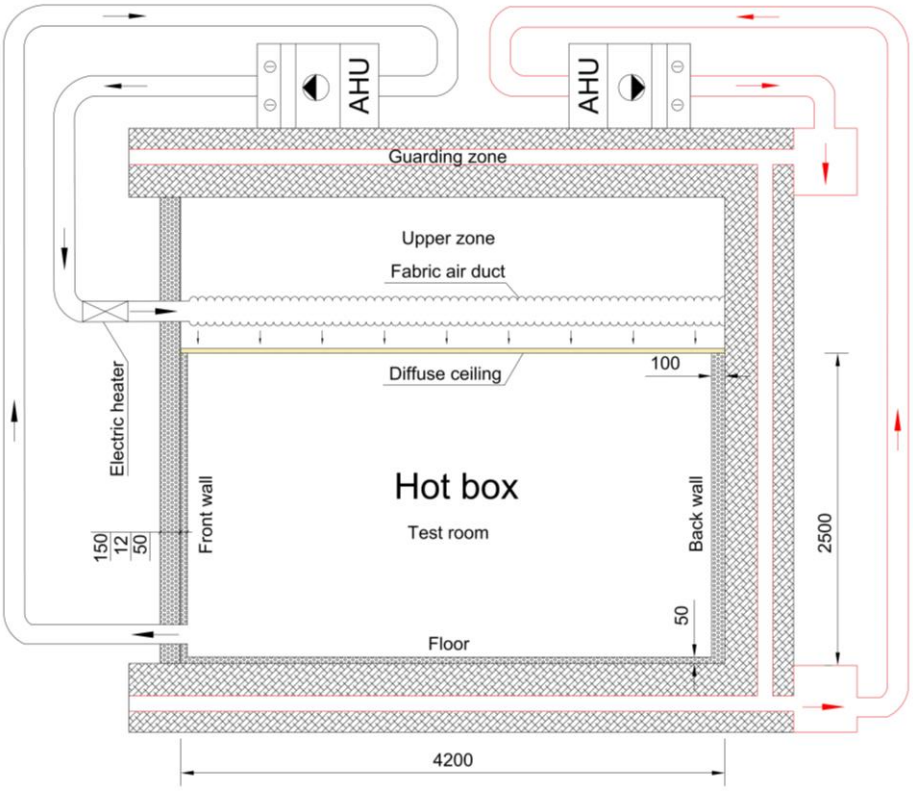


Fig. 1. Vertical section view of the hot box.

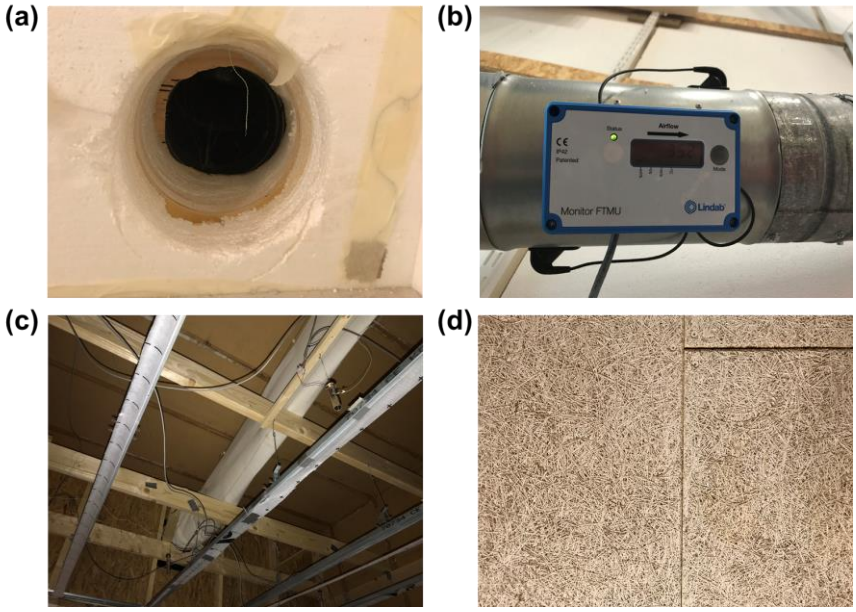


Fig. 2. (a) Outlet, (b) air distribution duct with airflow sensor, (c) fabric air duct and suspension brackets, and (d) diffuse ceiling panel.

## 2.2 Design cases and experimental procedure

The total dynamic heat capacity per unit floor area ($c_{dyn}/A_{floor}$) defines the building's thermal mass level. $c_{dyn}$ represents the amount of energy stored per surface area when the surface is exposed to a sinusoidal temperature variation over one periodic cycle and can be calculated by EN ISO 13786 [40]. The original test room's thermal mass level was low, with the $c_{dyn}/A_{floor}$ of 31.6 kJ/m$^2$·K. In order to investigate the influence of thermal mass distribution on the heat transfer in the test room, 18mm Fermacell® fiber plasterboards ($\rho$=1150 kg/m3, $C_p$=1100 J/kg·K, $\lambda$=0.32 W/m·K) were installed on the different surfaces of the test room or were used to assemble four tables in the room. Each table comprised two fiber plasterboards (i.e., 36 mm thickness) and was supported with four metal columns with a height of 700 mm. Fig. 3 shows the locations of tables. Three different constant air change rates per hour (ACH) and two initial temperature differences ($\Delta T_0$) between the supply air (i.e., the conditioned air before entering the plenum) and test room indoor air were designed for different experimental cases. Table 1 lists the design cases and the corresponding thermal mass level of the test room. For the sake

of simplification, the fiber plasterboard is called "thermal mass" in later sections. The design cases are referred to by abbreviations in later sections. For example, '10ACH 10°C Floor' represents case 1 with ACH of 10 $h^{-1}$, $\Delta T_0$ of 10°C, and thermal mass installed on the floor.

The experiment procedures are: (1) supplying the air temperature with 22 °C until the steady state was reached (i.e., interior surfaces and indoor air temperature were close to 22 °C, the average temperature difference between the interior and exterior surfaces less than 0.1 °C); (2) supplying the conditioned cold air with the predefined temperature to the upper zone and exhaust the air from the test room by AHU for 8 hours to simulate NV. Steps 1 and 2 were then repeated for the next case. An automatic control system was developed using the LabVIEW programming language to identify the steady state and control AHUs. It is worth noting that an electrical heater with a power of 1000 W was installed before the inlet of the upper zone (cf. Fig. 1). The heater was turned on to heat the conditioned air with predefined temperature (e.g., 12°C) to 22 °C to ensure steady state condition. Then the heater to start the NV case study. This is done to save the time to turn the temperature from 22 °C to the predefined temperature by AHU.

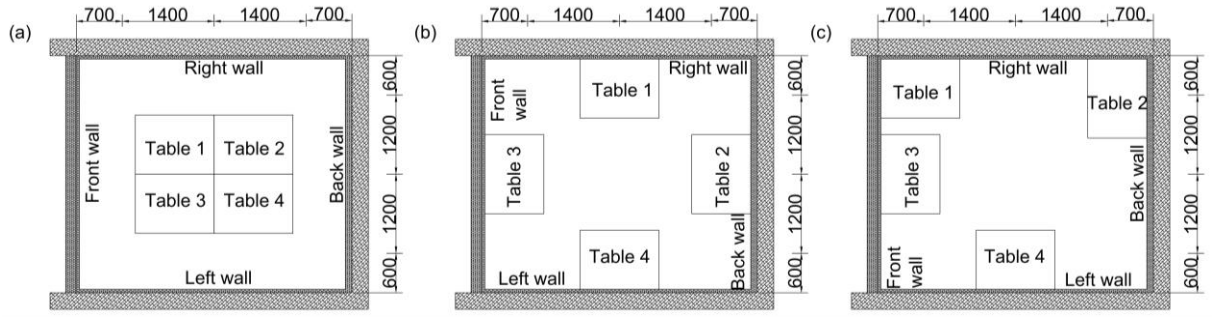


Fig. 3. Tables (a) in the middle, (b) close to walls, and (c) close to corners or walls.

Table 1. Design cases and the corresponding thermal mass level of the test room.

| Case No. | Thermal mass distribution | ACH ($h^{-1}$) | $\Delta T_0$ (°C) | Total $c_{dyn}/A_{floor}$ (kJ/m$^2$·K) |
|---|---|---|---|---|
| Case 1 to 6 | Floor | 10, 5, 2 | 10, 5 | 50.6 |
| Case 9 to 12 | Floor+Table(a) | 10, 5 | 10, 5 | 75.9 |
| Case 13 to 16 | Floor+Table(b) | 10, 5 | 10, 5 | 75.9 |

| | | | | |
|---|---|---|---|---|
| Case 17 | Floor+Table(c) | 10 | 10 | 75.9 |
| Case 18 | Floor+Table(c) | 5 | 5 | 75.9 |
| Case 19 | Floor+Right wall | 5 | 5 | 62.6 |
| Case 20 to 25 | Not installed | 10, 5, 2 | 10, 5 | 31.6 |

## 2.3 Measurements

Table 2 shows the specifications of measurement equipment and the measured parameters. Every surface in the test room was evenly divided into nine parts, and the center of each part was the measuring point for thermocouples or thermopiles (see Fig. 4a). A thermal paste ensured good thermal contact between the thermocouples and surfaces. Fig. 4b and c detail the locations of the thermocouples and thermopiles in one wall.

Table 2. Specification of measurement equipment.

| Instrument | Measured parameter | Range | Accuracy | Remark | Reference |
|---|---|---|---|---|---|
| FTMU UltraLink | Airflow rate | 0 to 507 $m^3/h$ | ±5% | Ø=160 mm | [41] |
| Type K thermocouple | Surface temperature, indoor air, and outlet temperature | 0 to 50 °C | ± 0.09 °C | | [42] |
| | Local air temperatures above and below the diffuse ceiling | | | With shielding ventilated tube | [43] |
| PT 100 | Supply air temperature, air temperature from AHUs | 0 to 50 °C | ±0.1 °C | | [44] |
| TH9100MR Thermo tracer | Diffuse ceiling temperature | -20 to 100 °C | ±2 °C | | [45] |
| Thermopile | Temperature difference between interior and exterior surface | - | ± 0.058 °C | Formed by 3 thermocouples connected in series | [46] |
| Hot-sphere Anemometer | Air velocity | 0 to 5 m/s | ± 0.05 m/s | - | [47] |

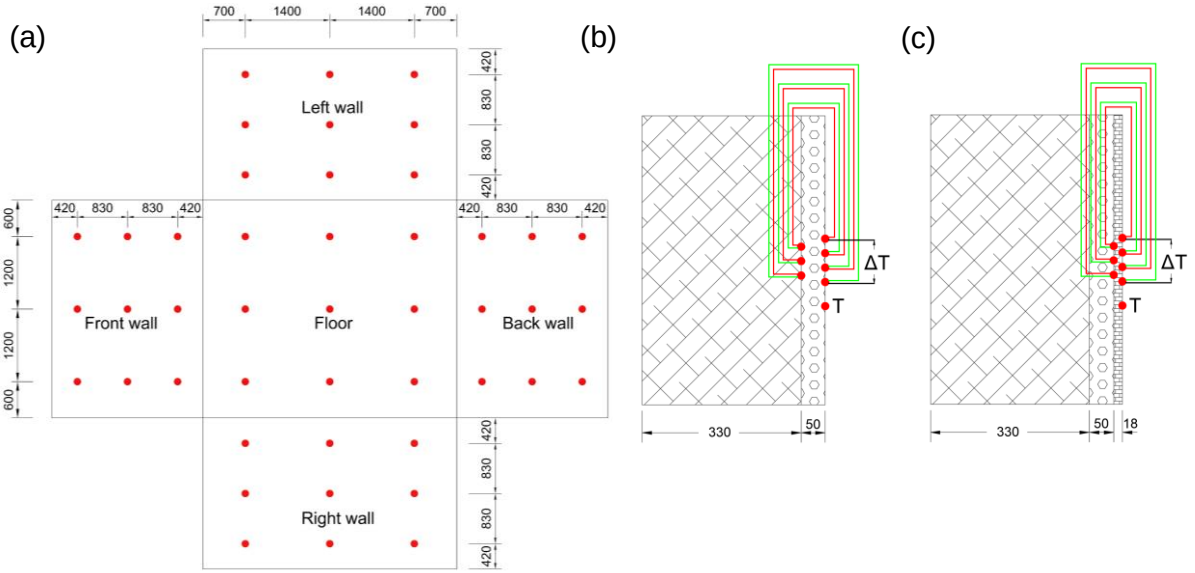


Fig. 4. (a) Positions of thermocouples/thermopiles measuring points in the surface, location of thermocouple and thermopile in (b) the original wall, (c) the original wall with fiber plasterboard.

Local air temperatures above and below the diffuse ceiling were measured by thermocouples. Fig. 5a and b show the horizontal section and vertical section of the temperature measuring points, respectively. The thermocouples shielded inside a ventilated tube (see Fig. 5c), which was formed by the silver and had a mini-fan inside to produce a low-speed airflow (1.5 m/s) to accurately measure the air temperature by reducing the error caused by radiation and increasing convection employing ventilation [43], as shown in Fig. 5c. The upper shielding ventilated thermocouples measured the inlet air temperature for the test room, while the temperatures measured by the lower shield thermocouples denote the diffuse ceiling lower surface temperatures. The reason is that the air temperature close to the diffuse ceiling lower surface was almost identical to the diffuse ceiling lower surface temperature under the summer cooling scenario with internal heat gains [37]. We infer those two temperatures should be closer under the NV scenario since no internal heat gains are present in the test room. A thermo tracer was used to measure surface emissivity (see Fig. 4d).

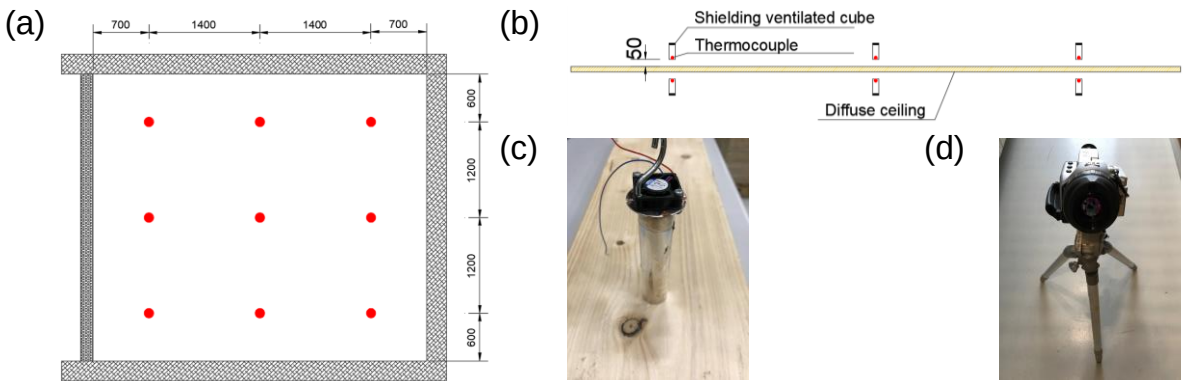


Fig. 5. (a) Horizontal section of measuring points below and above the diffuse ceiling, (b) vertical section of measuring points, (c) shielding ventilated tube, (d) thermo tracer.

Air velocities were measured by hot-sphere anemometers placed on the movable columns or interior surfaces. Fig. 6a shows the horizontal positions of anemometers in the test room, of which "A1 – A13" represents the positions of columns, and "B1 – B9" means the positions of anemometers placed on the ceiling and floor. The columns (A1 – A12) hold three anemometers, while the column (A13) only had one, as shown in Fig. 6b and c. Each position (B1 – B9) had two anemometers installed on the ceiling and floor, respectively. The distances of anemometers away from surfaces were 50 mm.

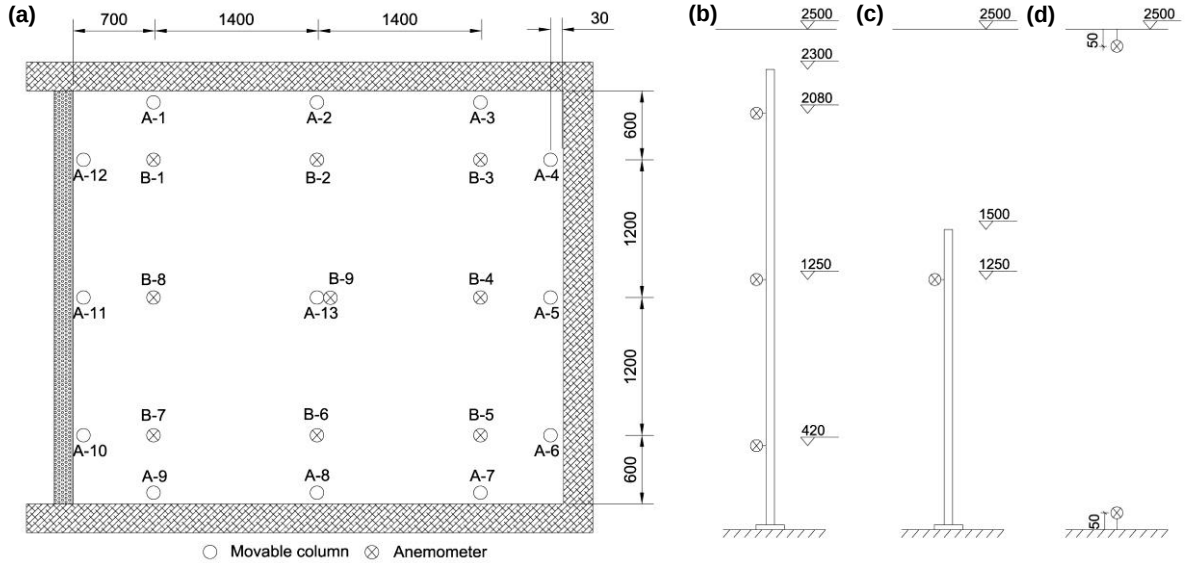

Fig. 6. (a) Horizontal positions of anemometers in the test room, (b) anemometers in the columns close to the room surface (A1-A12), (c) anemometer in the column in the middle of the room (A-13), (d) anemometers fixed close to the ceiling or floor (B1-B9).

One thermocouple located in the middle of the test room measured the indoor air temperature, while another one placed in the middle of the outlet recorded the outlet air temperature. Fluke Helios Plus 2287A dataloggers acquired analog signals from all thermocouples and thermopiles. PT100 monitoring the supply air temperature for the upper zone was logged with a data acquisition modules NI-9216 from National Instruments. The sampling rate of 0.1 Hz (every 10 s) was selected to log all the data. To reduce the noise in the measurement signals, the moving average of 15 values (2.5 min) was applied.

# 3 DATA ANALYSIS

## 3.1 Derivation of CHTC

The convective heat flux ($q_{\mathrm{conv},i}$) on surface $i$ is derived by the corresponding calculated conductive heat flux ($q_{\mathrm{cond},i}$) and radiative heat flux ($q_{\mathrm{rad},i}$) based on the inside surface heat balance, as shown in Eq. (1), assuming that heat flux from outside to inside is positive. Then, the convective heat transfer coefficient (CHTC) $h_{conv,i}$ at surface $i$ is calculated by Eq. (2).

$$q_{\mathrm{conv},i} = q_{\mathrm{cond},i} - q_{\mathrm{rad},i} \tag{1}$$

$$h_{conv,i} = \frac{q_{\mathrm{conv},i}}{(T_{\mathrm{ref}} - T_{\mathrm{surf},i})} \tag{2}$$

where $T_{\mathrm{ref}}$ and $T_{\mathrm{surf},i}$ are the reference temperature and surface $i$ temperature, respectively. $q_{\mathrm{cond},i}$ was calculated by a transient 1D finite difference model with an explicit scheme [48]. The boundary conditions for the 1D model were the interior and exterior surface temperatures, respectively. For the surfaces (i.e., four walls and the floor), the interior surface temperature was measured by the thermocouple, and the exterior surface temperature was derived by the

temperature difference measured by the thermopile and the measured interior surface temperature. For the four tables, the interior and exterior surface temperatures were measured by the thermocouples. $q_{\mathrm{rad},i}$ was calculated using the radiosity method [49] that is widely used in BES tools like EnergyPlus and IDA-ICE. Eq. (3) & (4) show the calculation method.

$$\left[\frac{\delta_{ij}-(1-\varepsilon_i)\cdot F_{i-j}}{\varepsilon_i}\right][J_i] = [E_{\mathrm{b}i}] \tag{3}$$

$$q_{\mathrm{rad},i} = \frac{\varepsilon_i}{(1-\varepsilon_i)} \cdot [E_{\mathrm{b}i} - J_i] \tag{4}$$

where $\delta$ is the Kronecker symbol, $\varepsilon$ is the emissivity, $F_{i-j}$ is view factor from surface $i$ to surface $j$ and $E_{\mathrm{b}}$ is the black body emissive power. For cases without indoor tables, $F_{i-j}$ was calculated by the method for perpendicular and parallel rectangular plates [50]. While for cases with tables, $F_{i-j}$ was considered as the obstructed view factor and was calculated using the adaptive integration method [51].

## 3.2 Uncertainty analysis

The uncertainty analysis based on the most widely used uncertainty propagation method-Monte Carlo analysis (MCA) was conducted to estimate the uncertainty of result concerning the accuracies of equipment (cf. Table 1) and the uncertainties of the material properties that were assumed to be normally distributed and given with a confidence interval of 95%, as shown in Table 3. The thermal conductivity, density, and specific heat capacity originated from the manufacture, while the emissivity was deduced by comparing the material surface temperature to the temperature of black tape with high emissivity using the TH9100MR thermo tracer. Latin Hypercube Sampling (LHS) was adopted as the sampling method to generate the input scenarios according to the uncertainties of parameters mentioned above. The benefit of LHS is that results can be converged easily with a considerably small reduced number of samples for the MCA [52]; thus, the sample size by LHS was set as 300. After generating input scenarios

by LHS, MCA was then conducted to determine the total uncertainty with a confidence interval of 95% for the derived results, including the CHTC.

Table 3. Properties of materials used in the test room.

| Material | λ (W/m·K) | $\rho$ (kg/m$^3$) | $C_p$ (J/kg·K) | $\varepsilon$ (-) |
|---|---|---|---|---|
| Wood-cement | 0.085 ± 0.001 | 359 ± 10 | 923 ± 100 | 0.95 ± 0.03 |
| Foam boards | 0.038 ± 0.001 | 14.5 ± 0.1 | 1500 ± 100 | 0.96 ± 0.03 |
| Fiber plasterboards | 0.32 ± 0.01 | 1150 ± 10 | 1100 ± 100 | 0.95 ± 0.03 |

## 3.3 General form of CHTC correlation development

Forced convection is the driving force of NV. For a flat plate with dominated forced convection, the Nusselt number ($Nu_H$) can be written as a function of the Reynolds number ($Re_H$) by Eq. (5) [53].

$$\frac{hH}{k} = \mathrm{Nu}_H \sim \begin{cases} \mathrm{Re}_H^{0.5}, \text{for larminar flow} \\ \mathrm{Re}_H^{0.8}, \text{for turbulent flow} \end{cases} \quad (5)$$

$$\mathrm{Re}_H = \frac{U_\infty H}{v} \quad (6)$$

where $h$ is the CHTC, $U_\infty$ represents the fluid free stream velocity, $H$ is the plate length, $k$ is the fluid thermal conductivity, $v$ is the air dynamic viscosity.

Fisher & Pedersen [54] conducted the steady-state experiment in an isothermal room with a radial ceiling diffuser that supplied air with ACH from 3 to 12 h$^{-1}$ and with the temperature from 10 °C to 25 °C to derive the CHTCs with the inlet temperature as the reference at interior surfaces. They then combined the experimental results with the high ACH from 15 to 100 h$^{-1}$ [21] to develop the correlations for forced convection in the enclosure by the scale analysis of the boundary layer for the flat plate in Eq. (5). Table 4 shows these correlations for forced convection.

Table 4. CHTC correlations for the radial ceiling diffuser configuration (ACH: 3 to 100 h$^{-1}$) [54].

| Surface type | Correlations |
|---|---|
| Ceiling | $h = 0.49ACH^{0.8}$ |
| Floor | $h = 0.13ACH^{0.8}$ |
| Walls | $h = 0.19ACH^{0.8}$ |

Fisher [55] also noticed that correlations in Table 4 gave a relatively large error in predicting the CHTC at low ACH due to the flow pattern not being fully turbulent. Then, a relationship between $\mathrm{Nu_e}$ and $\mathrm{Re_e}$ was expressed in Eq. (7).

$$\mathrm{Nu_e} = \mathrm{C_2} + \mathrm{C_3} \cdot \mathrm{Re_e^m} \tag{7}$$

$$\mathrm{Nu_e} = \frac{hL}{k} \tag{8}$$

$$\mathrm{Re_e} = \frac{\dot{m}}{\rho v L} \tag{9}$$

where $L$ is the characteristic length that can be the cubic root of the room volume ($V_{room}^{1/3}$), and $\dot{m}$ is the air volume flow rate. Combining Eqs. (7) to (9), the CHTC can be expressed by Eq. (10).

$$h = \mathrm{C_4} + \mathrm{C_5} \cdot ACH^m, 0.5 \leq m \leq 0.8 \tag{10}$$

Eq. (10) was used as the general form for the CHTC correlation development. The reference temperature for the correlation development was the inlet temperature for the test room (i.e., the temperature measured by shielding ventilated thermocouple above the diffuse ceiling panel, cf. Fig. 5b). It should be noticed that the CHTC at the diffuse ceiling lower surface (i.e., the ceiling for the test room) was not investigated. The reasons are listed below: (1) the convective heat flux at the diffuse ceiling surface is difficult to be derived because the porous matrix of wood-cement ceiling converts part of the conductive and convective heat transfer into radiative heat transfer [22]; (2) the diffuse ceiling made by the wood-cement has very low thermal mass and heat capacitance, which has little influence on the energy use of DCV with respect of the whole space; (3) the heat transfer through the porous material in BES tools like EnergyPlus cannot be modeled by the most commonly used Conduction Transfer Function (CTF) module.

While the Combined Heat and Moisture Transfer (HAMT) Model needs another input of moisture in all the building materials and does not fit the heat transfer equations for the diffuse ceiling panel mentioned in [22]. This is because EnergyPlus treats the air exchange and interchange between zones as convective heat gain [13]. A possible approach to select the suitable CHTC correlation for the diffuse ceiling is to adopt different existing correlations to find the one that minimizes the discrepancy between the measured values (e.g., interior surface temperature) and simulated values by BES.

After integrating the conductive and radiative heat flux at nine sections of each surface and calculating the mean surface temperature, Eq. (2) was used to calculate the surface-averaged CHTCs with the inlet temperature as the reference over the night cooling period. It is worth noting that the first hour data of the whole 8-hour night cooling period is excluded due to the initial transient effect at the beginning of NV.

The forced CHTC correlations for the floor and walls in Table 4 as well as the correlations in Table 5 that were derived from the same test chamber with a sidewall inlet, were used to compare with the experimental CHTCs. Petersen et al. [56] found that DCV tends to have the displacement ventilation effect within the occupied zone at low internal heat loads. Therefore, the forced convection correlation for the floor ($h = 0.48ACH^{0.8}$) without heat patches under the displacement ventilation was also selected for comparison [57].

Table 5. CHTC correlations for the sidewall inlet configuration (ACH: 3 to 12 $h^{-1}$) [55].

| **Surface type** | **Correlations** |
|---|---|
| Floor | $h = 0.698 + 0.173ACH^{0.8}$ |
| Wall | $h = -0.109 + 0.135ACH^{0.8}$ |

Furthermore, adaptive CHTC correlations that blended the natural and forced convection correlations [58] were also used for comparison. Those correlations may be the most comprehensive model for CHTC available and have been widely implemented in BES tools. For the NV scenario (i.e., cold air above or close to interior surfaces), the correlations for the

buoyant floor and the walls with opposing forces were selected, as shown in Eq. (11) and Eq. (12), respectively.

$$h_{\text{floor,adaptive}} = \left[\left[\left(1.4\left(\frac{\Delta T}{D_h}\right)^{1/4}\right)^6 + \left(1.63\Delta T^{1/3}\right)^6\right]^{3/6} + \left[\left(\frac{T_{surf}-T_{inlet}}{\Delta T}\right)(0.159 + 0.116ACH^{0.8})\right]^3\right]^{1/3} \quad (11)$$

$$h_{\text{wall,adaptive}} = \max\begin{cases}\left[\left[\left(1.5\left(\frac{\Delta T}{H}\right)^{1/4}\right)^6 + \left(1.23\Delta T^{1/3}\right)^6\right]^{3/6} - \left[\left(\frac{T_{surf}-T_{inlet}}{\Delta T}\right)(-0.199 + 0.19ACH^{0.8})\right]^3\right]^{1/3} \\ 80\%\left[\left(1.5\left(\frac{\Delta T}{H}\right)^{1/4}\right)^6 + \left(1.23\Delta T^{1/3}\right)^6\right]^{1/6} \\ 80\%\left[\left(\frac{T_{surf}-T_{inlet}}{\Delta T}\right)(-0.199 + 0.19ACH^{0.8})\right]\end{cases} \quad (12)$$

where $\Delta T$ is the temperature difference between the surface and the indoor air, $H$ is the wall height, and $D_h$ is the hydraulic diameter of the floor, which is calculated by 4×area/perimeter. It is worth noting that the outlet air temperature is selected to represent the test room's average indoor air temperature due to the small air temperature gradient in the ventilated room [37]. Therefore, the surfaced-average CHTCs with the outlet temperature as the reference were deduced to compare with the predicted values by adaptive correlations. The discrepancy between the two values was evaluated by the mean absolute percentage error (MAPE) using Eq. (13).

$$\text{MAPE} = \frac{1}{n}\sum_{t=1}^{n}\left|\frac{E_t - P_t}{E_t}\right| \quad (13)$$

where $E_t$ and $P_t$ are the experimental value and predicted value at point *t*, respectively. $n$ is the number of data points (i.e., 2520 points from 7h data with 10s interval). MAPE was also used to evaluate the discrepancy between the experimental CHTC (inlet temperature as reference) with predicted values by forced correlations at ACH of 5 and 10 $h^{-1}$.

The indoor furniture was usually regarded as a horizontal and upward-facing surface in BES software [34] because no specific CHTC correlations were developed for the furniture. Therefore, the forced correlations and adaptive correlations for the floor were also used for comparison, respectively.

# 4 RESULTS AND DISCUSSION

## 4.1 CHTC at the floor

Fig. 7 shows the experimental surface-averaged CHTCs at the floor (inlet temperature as reference) and the corresponding existing CHTC correlations. The nonlinear least square method with the trust-region-reflective [59] algorithm is adopted to deduce the fitted curve based on the experimental values. For different design cases, the $R^2$ (coefficient of determination) of fitted curves is between 0.90 and 0.94, and the uncertainties estimated for the surface-averaged CHTCs range from ± 6% to ± 10%. It is worth noting that there are two experimental values at the same ACH, representing the values are from two different inlet temperatures. Those values are very close to each other, indicating $\Delta T_0$ has little influence on the average CHTC at the floor; thus, demonstrating the inlet jet momentum by NV drives the forced convection at the floor.

It can be seen that at the same ACH, Novoselac et al.'s correlation [57] (i.e., displacement ventilation) predicts the highest CHTC, followed by Fisher's correlation [55] (i.e., sidewall inlet) and Fisher & Pedersen's correlation [54] (i.e., radial ceiling diffuser). The reason is that the displacement ventilation diffuser located on the floor covered a larger floor area with the cool inlet jet compared to the free horizontal jet from the vertical slot located in the middle of a west wall and the downward jet from the radial ceiling diffuser. When the thermal mass (i.e., fiber plasterboard) was installed on the floor (except Fig. 7f), the experimental values at ACHs of 5 and 10 $h^{-1}$ fit quite well with Fisher's correlation, while the other two existing correlations either overestimate or underestimate the experimental values. It seems that the presence of tables, locations of tables, and the thermal mass installed on the right wall has negligible impact on the average CHTC at the floor. Even though the number of experimental values for cases shown in Fig. 7b to Fig. 7e is smaller than the case with the thermal mass on the floor, it can infer that the fitted curve in Fig. 7a is also applicable for those cases with ACH ranging from 2

to 10 $h^{-1}$. Compared to the floor with thermal mass, the floor without thermal mass had much lower surface-averaged CHTCs (Fig. 7f). The possible reasons are: (1) the dynamic heat capacity of the floor increases a lot from 8.5 to 26.0 kJ/$m^2$·K by installing the thermal mass on the original foam boards, which provides a larger heat sink to store/release more heat; (2) the temperature congruence of the local air and floor surface is slowed down by the thermal mass which leads to a higher temperature difference for a longer period to extract more heat by NV. When no thermal mass is installed on the floor, all three existing correlations overestimate the average CHTC at the floor, of which Fisher & Pedersen's correlation predicted the results relatively well with the mean absolute percentage error (MAPE) of 38.7%, and root mean squared error (RMSE) calculated by Eq. (14) of 0.18 W/$m^2$·K at high ACH (i.e., 5 and 10 $h^{-1}$).

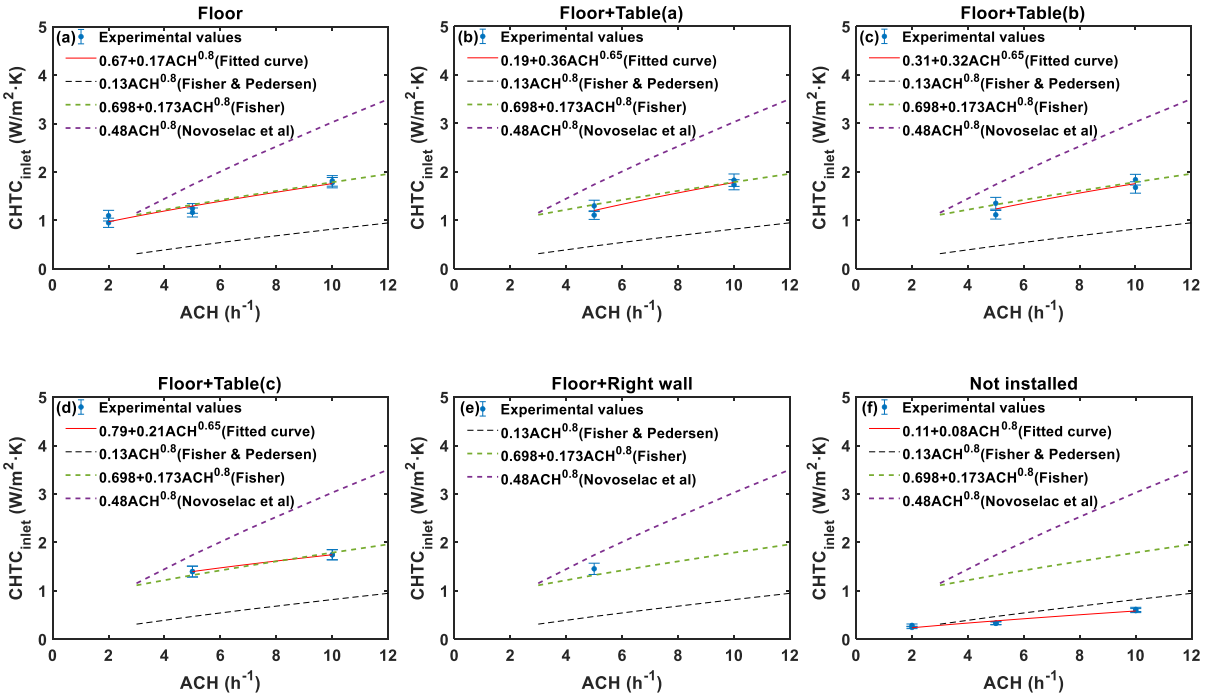


Fig. 7. Experimental CHTC at the floor for thermal mass on the (a) floor, (b) floor + table(a), (c) floor + table(b), (d) floor + table(c), (e) floor + right wall, and (j) thermal mass not installed.

$$\mathrm{RMSE} = \sqrt{\frac{\sum_{t=1}^{n}(E_t - P_t)^2}{n}} \quad (14)$$

The comparison between the experimental CHTCs at the floor (outlet temperature as reference) and the predicted CHTCs by the corresponding adaptive correlation is also conducted. Generally, the adaptive correlation for the floor underestimated the experimental values. The MAPE between those two values ranges from 42% to 221% for different design cases. The lowest MAPE (i.e., 42%) occurs in case 11 (5ACH 10 °C Floor+Table(a)), as shown in Fig. 8.

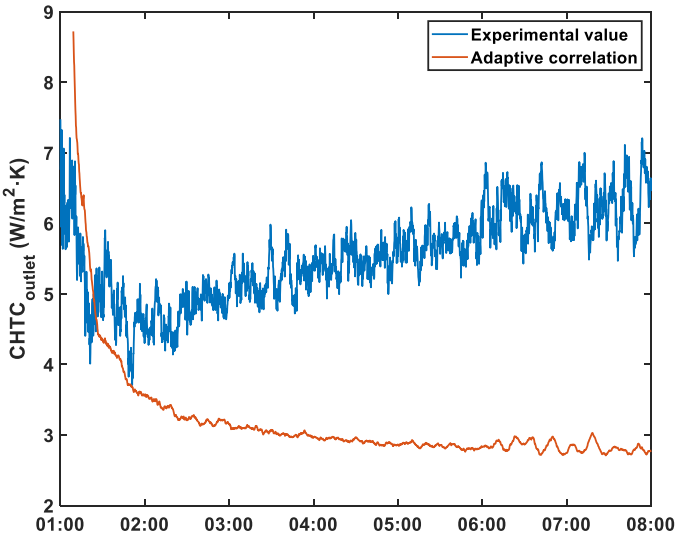


Fig. 8. Comparison between the experimental CHTC at the floor and CHTC predicted by adaptive correlation for the floor for case 11.

## 4.2 CHTC at walls

Fig. 9 shows the experimental surface-averaged CHTCs at four walls (inlet temperature as reference) and the corresponding two existing CHTC correlations. The experimental values with the same symbols at the same ACH represent those values are from two different inlet temperatures. The text of "Floor" or "Floor+Table(a)" in the legend of Fig. 9 represents the thermal mass distribution. The uncertainties estimated for the experimental CHTCs range from ± 5% to ± 10%. Fisher's correlation gives higher values for walls than Fisher & Pedersen's correlation at the same ACH because the jet from the radial ceiling diffuser covered a larger wall area than the free horizontal jet from the middle of a west wall. Fisher's correlation fits relatively better with the experimental values than Fisher & Pedersen's correlation, but the

errors are still large with MAPE ranging from 28% to 131%, and RMSE ranging from 0.17 to 0.34 $W/m^2 \cdot K$ for different walls at high ACH.

Fig. 10 shows the mean vertical air velocity measured by anemometers on columns A-1 to A-13 and anemometers in position B-9 (cf. Fig. 6) for case 1 (10ACH 10°C Floor) over the night cooling period. The vertical velocity changed little for most locations, indicating a relatively uniform air distribution in the test room. The velocity in the height of 0.42 m of column A-12 was larger than other measured velocities because the anemometer was close to the outlet. Due to the relatively uniform air distribution, the experimental CHTCs at four walls under the same ACH were similar, except the front wall had slightly higher CHTC than the other three walls for most cases. The reason could be that the outlet was located in the bottom right corner of the front wall that induced more airflow near the outlet, resulting in a higher average velocity over the entire front wall than other walls. Fig. 11 shows the local air velocity over the whole front wall with the linear interpolation and extrapolation method by the local velocities measured by nine anemometers on the columns A-10, A-11, and A-12 in Fig. 6 and the outlet velocity deduced by the airflow rate and outlet area for case 1 (10ACH 10°C Floor) after two hours, which supports the reasons mentioned above.

In Fig. 9b, it can be seen that the right wall with the thermal mass had a much higher average CHTC than the right wall without thermal mass, indicating the thermal mass enhanced the convective heat transfer at the surface. For cases without tables, the experimental values at the same ACH and under the same thermal mass distribution were almost independent of the inlet temperatures. The corresponding fitted curves with $R^2$ ranging from 0.91 to 0.95 (see Table 6). The presence of tables and the location of tables seem to have some influence on the average CHTC at walls. For cases with tables, the discrepancy between the experimental values with different inlet temperatures under the same locations of tables at the ACH of 10 $h^{-1}$ is large, with the absolute error up to 0.5 $W/m^2 \cdot K$, resulting in a small $R^2$ as low as 0.47. This may be

explained that tables obstructed the downward airflow to turn more airflow horizontal to walls or just reduced the downward airflow along the walls, changing the airflow pattern on the walls with different inlet temperatures. Therefore, the average CHTCs at walls are difficult to be predicted when tables are placed in the room.

An alternative easier way is to derive the fitted curve for each wall based on all experimental CHTCs regardless of the tables' parameters. The solid red lines in Fig. 9 are the fitted curves with $R^2$ ranging from 0.49 to 0.79. The $R^2$ of those fitted curves is small, leading to the MAPE between the experimental values and predicted values range from 17% to 51%. However, the RMSE between those two values ranges from 0.06 to 0.12 W/m$^2$·K, which should be acceptable in BES.

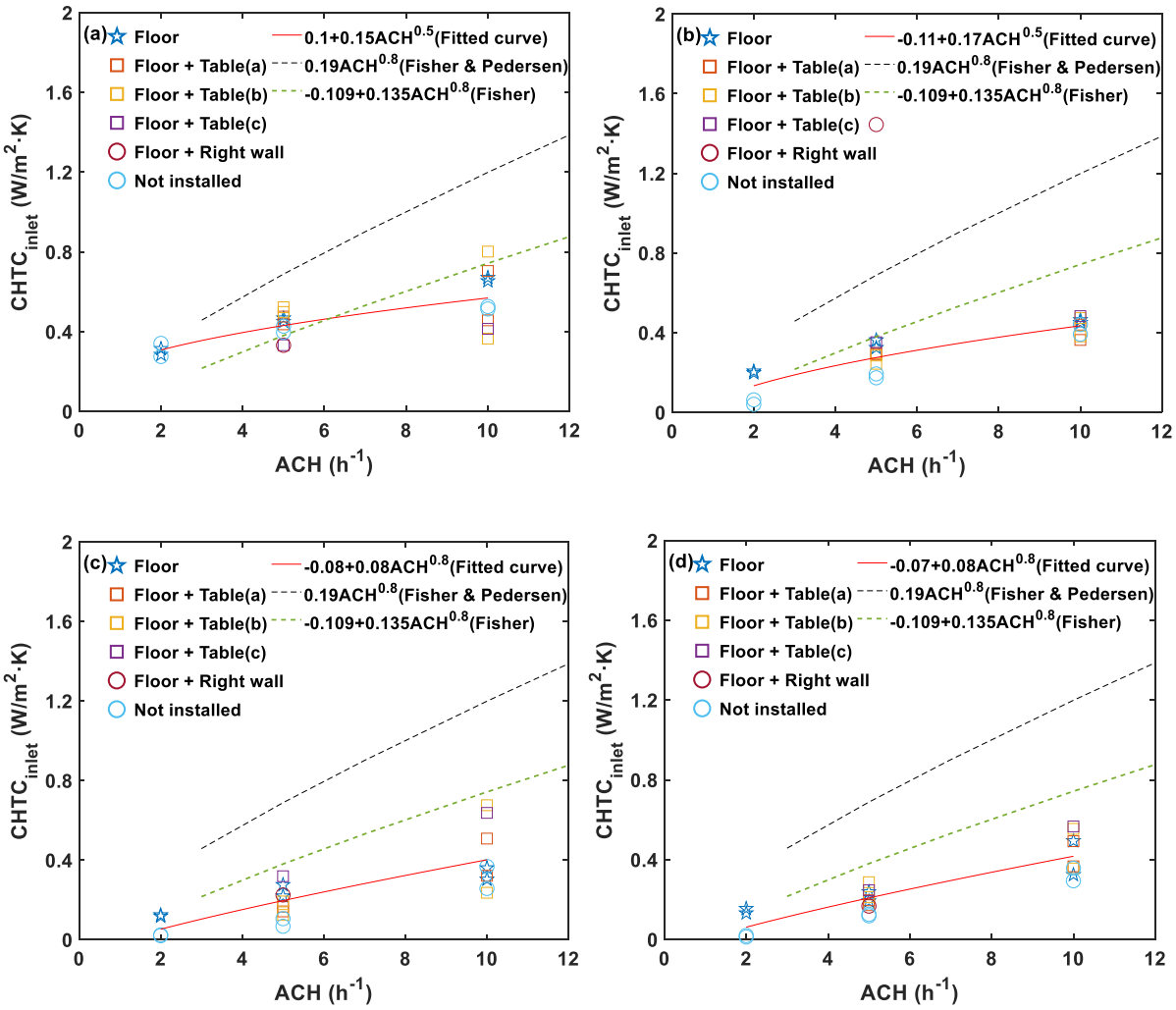


Fig. 9. Experimental CHTC at the (a) front wall, (b) right wall, (c) back wall, (d) left wall.

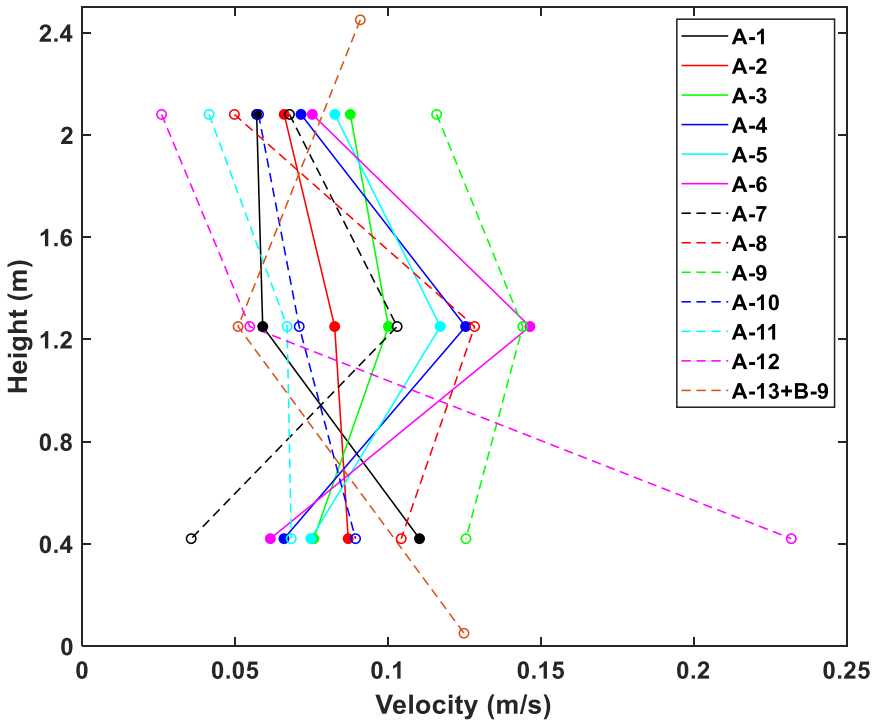


Fig. 10. Vertical air velocity measured by anemometers on columns A-1 to A-13 and anemometers in position B-9.

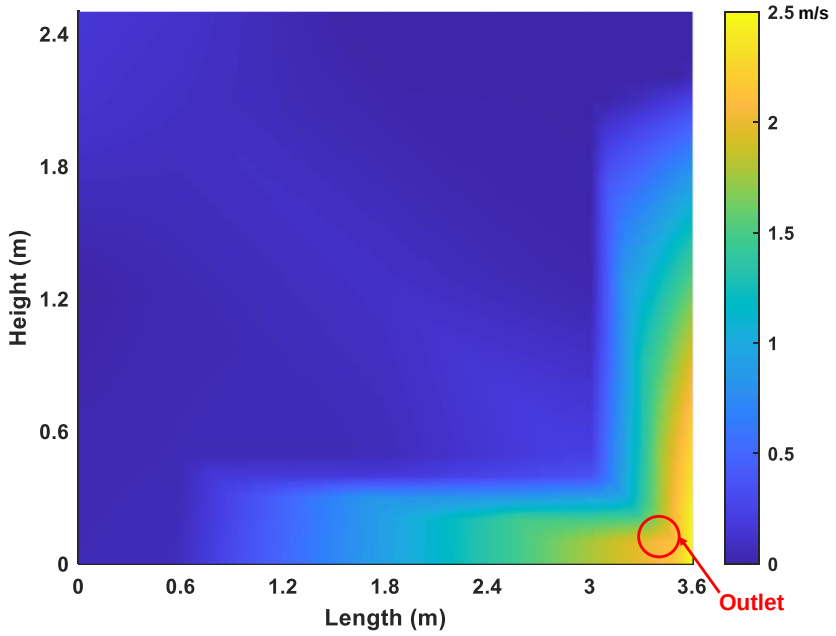


Fig. 11. Local air velocity over the front wall for case 1 after two hours.

Table 6. Fitted curve functions for CHTCs at different walls of two thermal mass distribution.

| Thermal mass distribution | Front wall | Right wall | Back wall | Left wall |
|---|---|---|---|---|
| Floor | $0.14+0.08ACH^{0.8}$ | $0.01+0.15ACH^{0.8}$ | $-0.04+0.12ACH^{0.5}$ | $0.03+0.06ACH^{0.8}$ |

| | | | | |
|---|---|---|---|---|
| Not installed | $0.14+0.12ACH^{0.5}$ | $-0.1+0.08ACH^{0.8}$ | $-0.15+0.07ACH^{0.8}$ | $-0.2+0.08ACH^{0.8}$ |

The comparison between the experimental CHTCs at four walls (outlet temperature as reference) and the predicted CHTCs by the corresponding adaptive correlation shows that the MAPE between those two values ranges from 14% to 3,229%. The reason that the MAPE can be up to 3,229% was that the experimental values of cases at low ACH were small, but the values predicted by adaptive correlations were large, leading to a small denominator and a large numerator for calculating the MAPE by Eq. (13). Either the adaptive correlation for the wall underestimated or overestimated the experimental values for different design cases. The lowest MAPE (i.e., 14%) occurs in case 9 (10ACH 10°C Floor+Table(a)) for the front wall, as shown in Fig. 12.

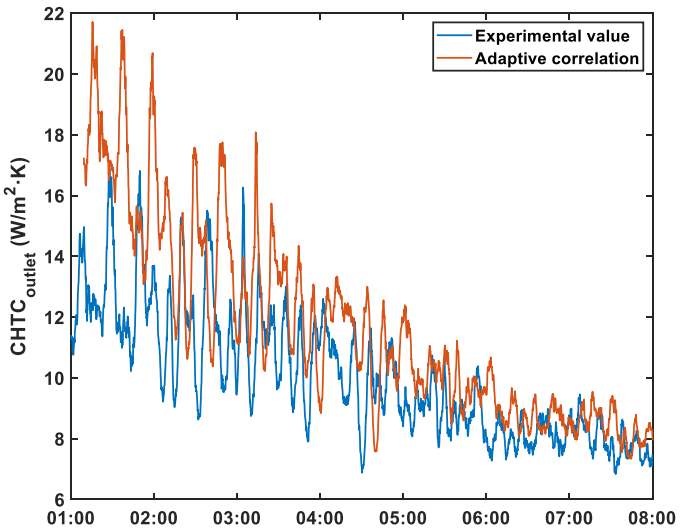


Fig. 12. Comparison between the experimental CHTC at the front wall and CHTC predicted by adaptive correlation for the wall for case 9.

## 4.3 CHTC at tables

Fig. 13 shows the surface-averaged CHTCs at tables (inlet temperature as reference) and the corresponding three existing correlations. The experimental values with the same symbols at the same ACH represent those values are from two different inlet temperatures. The uncertainties estimated for the surface-averaged CHTCs range from ± 7% to ± 12%. Fisher &

Pedersen's correlation predicts relatively well for CHTCs at table surfaces facing upward, while all three correlations largely overestimate the experimental values at table surfaces facing downward.

For the same table of all design cases, the CHTC at the table surface facing upward was higher than that for the table surface facing downward. Because the inlet jet poured down the table surface facing upward firstly and flowed over the table surface facing upward, while the table surface facing downward was affected relatively less by the cold air. Another reason that can contribute to the difference between the CHTCs at two surfaces of one table was the different view factor of the two surfaces, resulting in different radiative heat transfer fluxes, which can impact the CHTC. The CHTCs at tables were dependent on the locations of tables. However, it is difficult to develop an accurate CHTC correlation (i.e., $R^2$ exceeds 0.90) using the curve fitting method for specific locations of tables since the discrepancy between the experimental values at the same ACH with different inlet temperatures is high. The possible reason is that the boundary conditions for the 1D finite-difference model to calculate the transient conductive heat flux of table surfaces were temperatures measured by two thermocouples, causing higher uncertainty for the results than the other interior surfaces (e.g., floor) whose temperature difference was measured by thermopiles.

A feasible way is to derive the fitted curves (even with the small $R^2$ of 0.28 and 0.37, respectively) for table surfaces facing upward and for table surfaces facing downward based on the corresponding experimental values without concerning the location of tables, as shown in Table 7. The MAPE and RMSE between the experimental CHTCs at table surfaces facing upward and the CHTCs calculated by the fitted curves are 29% and 0.21 W/m$^2$·K. For table surfaces facing downward, the MAPE between the experimental values and predicted values are very large (up to 7,014%) because some experimental values are close to 0, but the RMSE between those two values is 0.13 W/m$^2$·K, which should also be acceptable in BES.

1

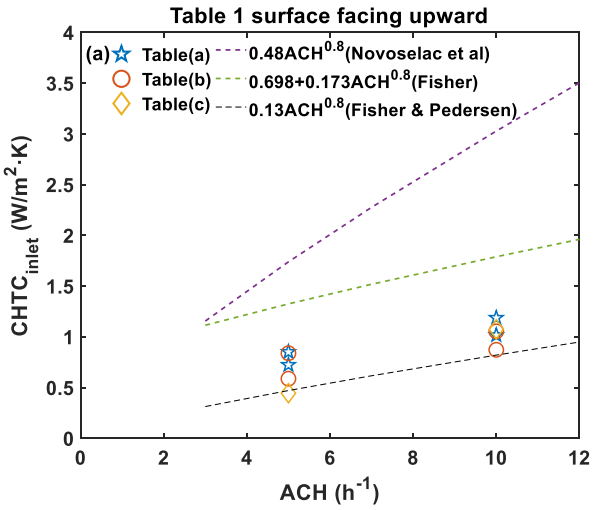
Table 1 surface facing upward
(a)
Table(a)
Table(b)
Table(c)
0.48ACH^0.8(Novoselac et al)
0.698+0.173ACH^0.8(Fisher)
0.13ACH^0.8(Fisher & Pedersen)
CHTC_inlet (W/m^2·K)
ACH (h^-1)

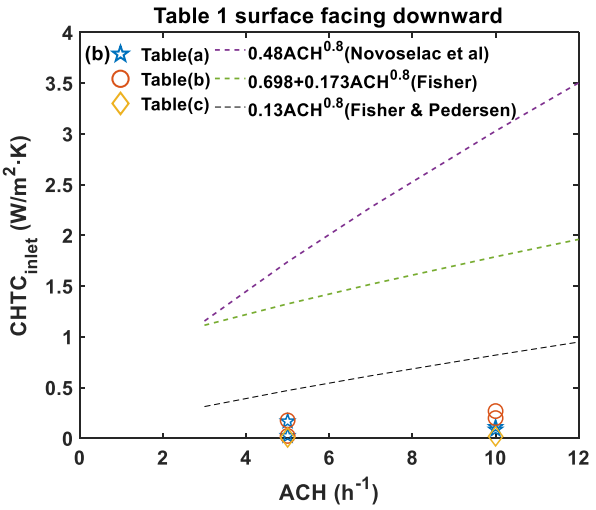
Table 1 surface facing downward
(b)
Table(a)
Table(b)
Table(c)
0.48ACH^0.8(Novoselac et al)
0.698+0.173ACH^0.8(Fisher)
0.13ACH^0.8(Fisher & Pedersen)
CHTC_inlet (W/m^2·K)
ACH (h^-1)

2

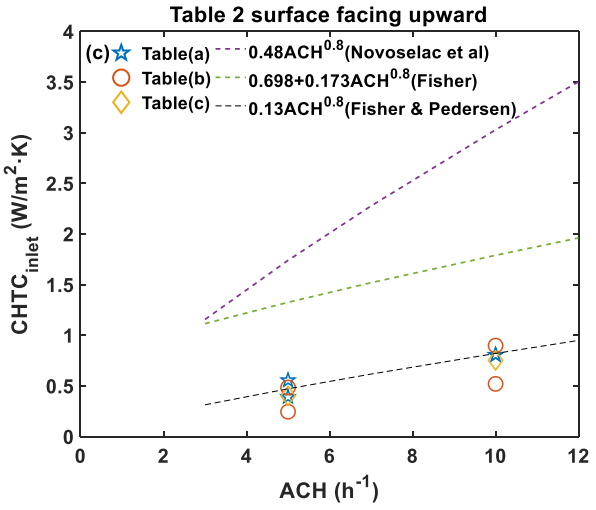
Table 2 surface facing upward
(c)
Table(a)
Table(b)
Table(c)
0.48ACH^0.8(Novoselac et al)
0.698+0.173ACH^0.8(Fisher)
0.13ACH^0.8(Fisher & Pedersen)
CHTC_inlet (W/m^2·K)
ACH (h^-1)

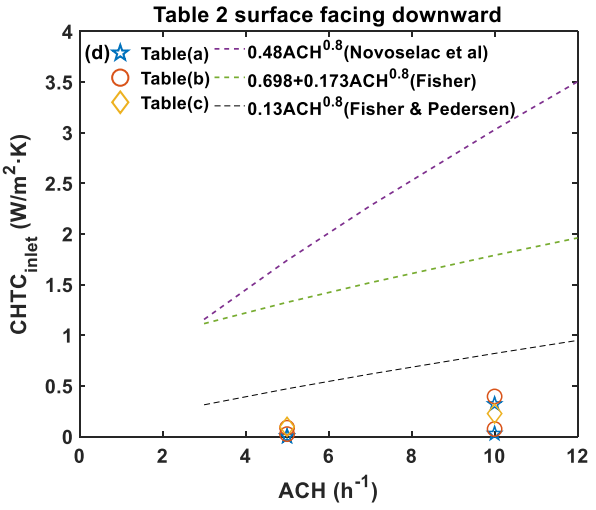
Table 2 surface facing downward
(d)
Table(a)
Table(b)
Table(c)
0.48ACH^0.8(Novoselac et al)
0.698+0.173ACH^0.8(Fisher)
0.13ACH^0.8(Fisher & Pedersen)
CHTC_inlet (W/m^2·K)
ACH (h^-1)

3

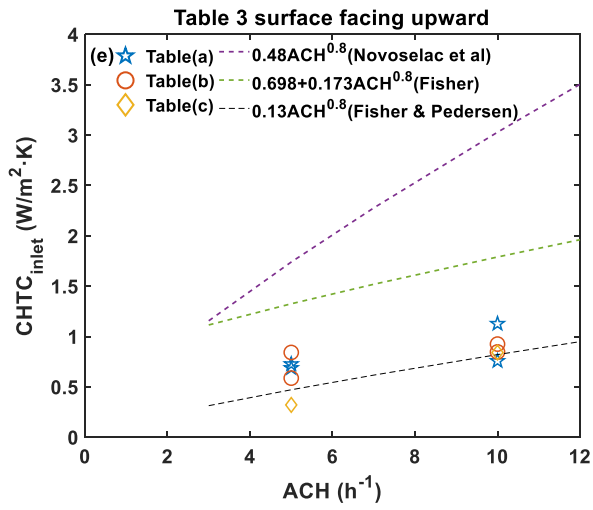
Table 3 surface facing upward
(e)
Table(a)
Table(b)
Table(c)
0.48ACH^0.8(Novoselac et al)
0.698+0.173ACH^0.8(Fisher)
0.13ACH^0.8(Fisher & Pedersen)
CHTC_inlet (W/m^2·K)
ACH (h^-1)

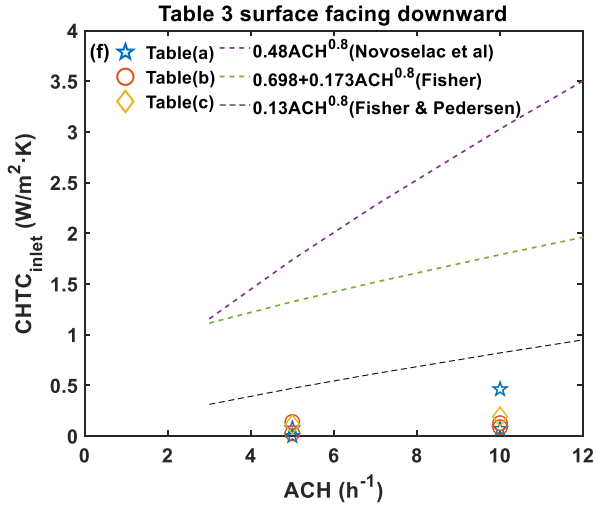
Table 3 surface facing downward
(f)
Table(a)
Table(b)
Table(c)
0.48ACH^0.8(Novoselac et al)
0.698+0.173ACH^0.8(Fisher)
0.13ACH^0.8(Fisher & Pedersen)
CHTC_inlet (W/m^2·K)
ACH (h^-1)

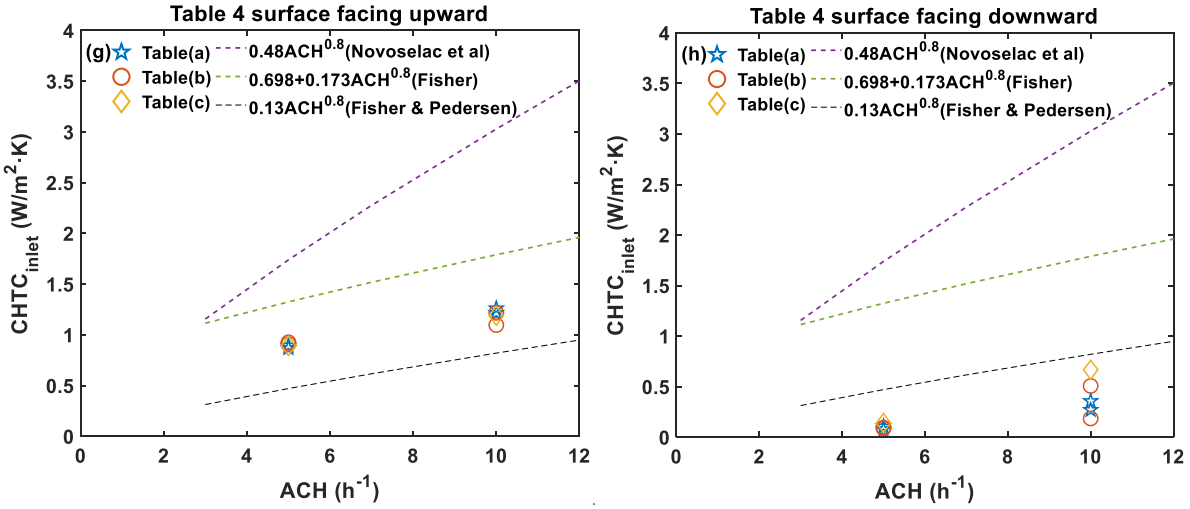


Fig. 13. Experimental CHTC at different table surfaces.

Table 7. Fitted curve functions for the table surface facing upward and downward.

| Table surface | Fitted curve function |
|---|---|
| Facing upward | $0.11+0.19ACH^{0.65}$ |
| Facing downward | $-0.21+0.1ACH^{0.65}$ |

The MAPE between the experimental CHTC at tables (outlet temperature as reference) and the predicted CHTC by the adaptive correlation for the floor range from 18% to 31,512%. Either the adaptive correlation for the floor underestimated or overestimated the experimental values for different design cases. The lowest MAPE (i.e., 18%) occurs in case 17 (10ACH 10°C Floor+Table(c)) for table 1 upward. The MAPE is up to 31,512% because the experimental CHTCs (outlet temperature as the reference) at the table surfaces facing downward were too small.

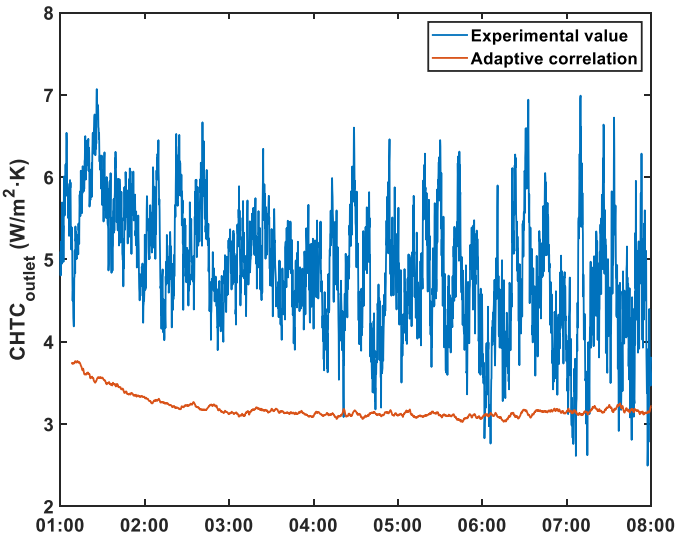


Fig. 14. Comparison between the experimental CHTC at table 1 surface facing upward and CHTC predicted by adaptive correlation for the floor for case 17.

## 4.4 Temperature efficiency

Apart from modeling the NV for performance estimation by adopting CHTC correlations in BES tools, the NV performance in terms of the surface cooling effectiveness can also be calculated in a simple model with the climatic cooling potential (CCP), temperature efficiency, and other parameters at the design stage [15]. The CCP for passive cooling of buildings by NV in Europe can be found in [60], while the temperature efficiency can be calculated by Eq. (15).

$$\eta = \frac{T_{\text{outlet}} - T_{\text{inlet}}}{\bar{T}_{\text{surface}} - T_{\text{inlet}}} \tag{15}$$

where $T_{\text{outlet}}$ and $T_{\text{inlet}}$ are the outlet and inlet temperatures, respectively. $\bar{T}_{\text{surface}}$ is the average interior surface temperature. Because the value of temperature efficiency oscillated during the cooling period, the $\eta$ for each case can be yielded by averaging the values over the cooling period (the first hour data excluded). Fig. 15 shows the temperature efficiencies of cases with the thermal mass on the floor and without thermal mass and corresponding fitted curves ($R^2 > 0.94$) based on the quadratic polynomial form. The fitted curves can be used to estimate the $\eta$ at other ACH. The uncertainties estimated for the $\eta$ range from ± 3% to ± 5%. It can be seen

that $\eta$ can be higher than 1 at low ACH. The temperature efficiency decreases with the increase of ACH, $\Delta T_0$ (i.e., the initial temperature difference between the supply air and indoor air), and thermal mass level. When comparing to the derived $\eta$ of the displacement ventilation and mixing ventilation in literature [15], the temperature efficiency of DCV is higher than those two ventilation concepts, except for the case with displacement ventilation at low ACH whose $\eta$ is higher than 1.10.

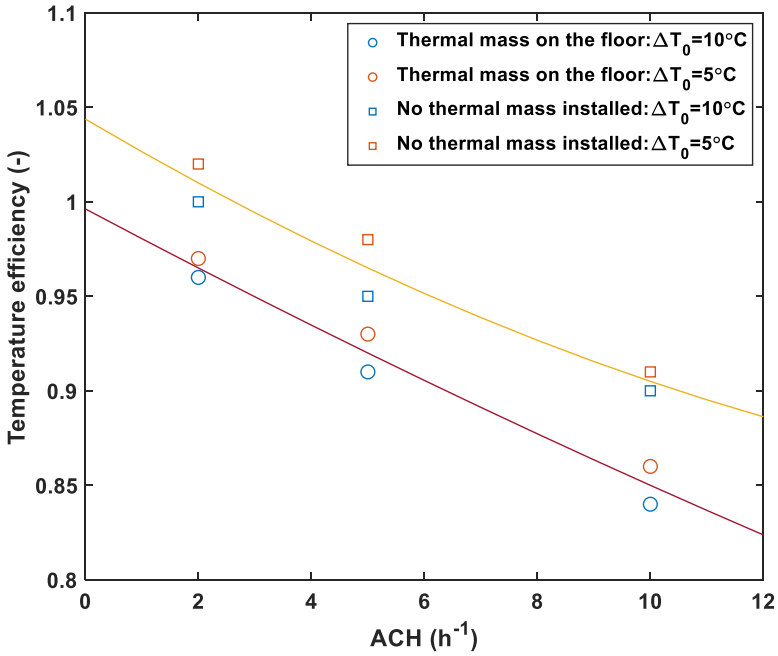


Fig. 15. Temperature efficiency depending on the ACH for DCV.

# 5 CONCLUSIONS AND FUTURE WORK

The heat transfer of night ventilation (NV) using the diffuse ceiling ventilation (DCV) concept was investigated by conducting a series of dynamic full-scale experiments. The design cases comprised 6 thermal mass distributions, 3 constant air change rates per hour (ACH), and 2 supply air temperatures. The surface-averaged convective heat transfer coefficient (CHTC) with the inlet temperature and outlet temperature as the reference at the floor, walls, and tables were derived from the experiments and compared with existing CHTC correlations. New CHTC correlations (inlet temperature as reference) specific to DCV with NV were developed. The

temperature efficiency of DCV was also derived to compare with that of the mixing ventilation and displacement ventilation.

For the surface-averaged CHTCs with the outlet temperature as the reference, the adaptive correlations predict accurately for some cases with a mean absolute percentage error (MAPE) between the experiment and the prediction as low as 14%. However, for most cases, large error was observed with MAPE up to 31,512%. For the surface-averaged CHTCs with the inlet temperature as the reference, existing forced correlations also do not predict well except Fisher's correlation (i.e., sidewall inlet configuration) for the floor [55], which predicts quite well for the floor with thermal mass. The presence of furniture (tables), its location, and the thermal mass installed on the wall have little influence on the CHTC at the floor. Increasing the thermal mass level of one surface can significantly augment the CHTC at the surface.

The temperature efficiency of DCV decreases with the increase of ACH, the initial temperature difference between the supply air and indoor air, and the thermal mass level. Compared to the temperature efficiency of mixing ventilation and displacement ventilation in literature, DCV has higher temperature efficiency in most cases, except the case with displacement ventilation at low ACH.

The developed CHTC correlations can be adopted in building energy simulation (BES) tools that enable the user to set custom functions for interior CHTC to simulate the building energy use and indoor thermal comfort quickly and more accurately without coupling complex computational fluid dynamics (CFD). Furthermore, the developed correlations also enable the user to optimize the ACH and thermal mass distribution to achieve low building energy use and good thermal comfort.

The study is limited because only two surface materials were used. The CHTC of the interior surface with other materials include PCM, needs to be investigated in the future. The influence of the plenum's height on the CHTCs of room interior surfaces also needs further study. CFD

simulations can be used to calculate the indoor temperature accurately. The latter can be regarded as the reference temperature to calculate the experimental CHTC and compare the adaptive correlations in this way. Due to the lack of CHTC correlation development for the suspended ceiling panel in this study, the suitable correlation for the diffuse ceiling in BES needs further research.

# 6 ACKNOWLEDGEMENTS

The project is carried out as part of IEA EBC Annex 80 Resilient Cooling. The first author gratefully acknowledges the financial support from the Chinese Scholarship Council (CSC No. 201706050001). The first author would also like to thank Lars Isbach Poulsen, Yanmin Wang, Bolong Wei, Baoming Su, Weiheng Zhang, and Min Liu for their great technical support.

# 7 REFERENCES

[1] E. Solgi, Z. Hamedani, R. Fernando, H. Skates, N.E. Orji, A literature review of night ventilation strategies in buildings, Energy Build. 173 (2018) 337–352. doi:10.1016/j.enbuild.2018.05.052.

[2] M. Kolokotroni, P. Heiselberg, Ventilative Cooling: State-of-the-Art Review, Aalborg Univ. Aalborg, Denmark. (2015). https://www.buildup.eu/en/node/52462.

[3] E. Solgi, Z. Hamedani, R. Fernando, B. Mohammad Kari, H. Skates, A parametric study of phase change material behaviour when used with night ventilation in different climatic zones, Build. Environ. 147 (2019) 327–336. doi:10.1016/j.buildenv.2018.10.031.

[4] S.P. Corgnati, A. Kindinis, Thermal mass activation by hollow core slab coupled with night ventilation to reduce summer cooling loads, Build. Environ. 42 (2007) 3285–3297. doi:10.1016/j.buildenv.2006.08.018.

[5] E. Solgi, Z. Hamedani, R. Fernando, B. Mohammad Kari, A parametric study of phase change material characteristics when coupled with thermal insulation for different Australian climatic zones, Build. Environ. (2019). doi:10.1016/j.buildenv.2019.106317.

[6] R. Lapisa, E. Bozonnet, P. Salagnac, M.O. Abadie, Optimized design of low-rise commercial buildings under various climates – Energy performance and passive cooling strategies, Build. Environ. (2018). doi:10.1016/j.buildenv.2018.01.029.

[7] E. Shaviv, A. Yezioro, I.G. Capeluto, Thermal mass and night ventilation as passive

cooling design strategy, Renew. Energy. 24 (2001) 445–452. doi:10.1016/S0960-1481(01)00027-1.

[8] R. Guo, P. Heiselberg, Y. Hu, C. Zhang, S. Vasilevskis, Optimization of night ventilation performance in office buildings in a cold climate, Energy Build. 225 (2020) 110319. doi:10.1016/j.enbuild.2020.110319.

[9] N. Artmann, H. Manz, P. Heiselberg, Parameter study on performance of building cooling by night-time ventilation, Renew. Energy. 33 (2008) 2589–2598. doi:10.1016/j.renene.2008.02.025.

[10] R. Guo, Y. Hu, M. Liu, P. Heiselberg, Influence of design parameters on the night ventilation performance in office buildings based on sensitivity analysis, Sustain. Cities Soc. 50 (2019) 101661. doi:10.1016/j.scs.2019.101661.

[11] K. Goethals, H. Breesch, A. Janssens, Sensitivity analysis of predicted night cooling performance to internal convective heat transfer modelling, Energy Build. 43 (2011) 2429–2441. doi:10.1016/j.enbuild.2011.05.033.

[12] L. Peeters, I. Beausoleil-Morrison, A. Novoselac, Internal convective heat transfer modeling: Critical review and discussion of experimentally derived correlations, Energy Build. 43 (2011) 2227–2239. doi:10.1016/j.enbuild.2011.05.002.

[13] U.S. DoE, Energyplus engineering reference, 2020. https://bigladdersoftware.com/epx/docs/9-3/engineering-reference/.

[14] J. Le Dréau, P. Heiselberg, R.L. Jensen, Experimental investigation of convective heat transfer during night cooling with different ventilation systems and surface emissivities, Energy Build. 61 (2013) 308–317. doi:10.1016/j.enbuild.2013.02.021.

[15] N. Artmann, R.L. Jensen, H. Manz, P. Heiselberg, Experimental investigation of heat transfer during night-time ventilation, Energy Build. 42 (2010) 366–374. doi:10.1016/j.enbuild.2009.10.003.

[16] W. Ji, Q. Luo, Z. Zhang, H. Wang, T. Du, P.K. Heiselberg, Investigation on thermal performance of the wall-mounted attached ventilation for night cooling under hot summer conditions, Build. Environ. 146 (2018) 268–279. doi:10.1016/j.buildenv.2018.10.002.

[17] D. Olsthoorn, F. Haghighat, A. Moreau, G. Lacroix, Abilities and limitations of thermal mass activation for thermal comfort, peak shifting and shaving: A review, Build. Environ. 118 (2017) 113–127. doi:10.1016/J.BUILDENV.2017.03.029.

[18] K. Goethals, I. Couckuyt, T. Dhaene, A. Janssens, Sensitivity of night cooling performance to room/system design: Surrogate models based on CFD, Build. Environ.

58 (2012) 23–36. doi:10.1016/j.buildenv.2012.06.015.
[19] K. Goethals, M. Delghust, G. Flamant, M. De Paepe, A. Janssens, Experimental investigation of the impact of room/system design on mixed convection heat transfer, Energy Build. 49 (2012) 542–551. doi:10.1016/j.enbuild.2012.03.017.
[20] P. Wallentén, Convective heat transfer coefficients in a full-scale room with and without furniture, Build. Environ. 36 (2001) 743–751. doi:10.1016/S0360-1323(00)00070-6.
[21] J.D. Spitler, C.O. Pedersen, D.E. Fisher, Interior convective heat transfer in buildings with large ventilative flow rates, in: ASHRAE Trans., 1991: pp. 505–515. www.hvac.okstate.edu (accessed May 11, 2020).
[22] W. Wu, N. Yoon, Z. Tong, Y. Chen, Y. Lv, T. Ærenlund, J. Benner, Diffuse ceiling ventilation for buildings: A review of fundamental theories and research methodologies, J. Clean. Prod. 211 (2019) 1600–1619. doi:10.1016/j.jclepro.2018.11.148.
[23] B. Yang, A.K. Melikov, A. Kabanshi, C. Zhang, F.S. Bauman, G. Cao, H. Awbi, H. Wigö, J. Niu, K.W.D. Cheong, K.W. Tham, M. Sandberg, P.V. Nielsen, R. Kosonen, R. Yao, S. Kato, S.C. Sekhar, S. Schiavon, T. Karimipanah, X. Li, Z. Lin, A review of advanced air distribution methods - theory, practice, limitations and solutions, Energy Build. 202 (2019) 109359. doi:10.1016/j.enbuild.2019.109359.
[24] C. Zhang, M.H. Kristensen, J.S. Jensen, P.K. Heiselberg, R.L. Jensen, M. Pomianowski, Parametrical analysis on the diffuse ceiling ventilation by experimental and numerical studies, Energy Build. 111 (2016) 87–97. doi:10.1016/j.enbuild.2015.11.041.
[25] P. V Nielsen, E. Jakubowska, The Performance of Diffuse Ceiling Inlet and other Room Air Distribution Systems, Cold Clim. HVAC. (2009) 7.
[26] J. Hu, P. Karava, Model predictive control strategies for buildings with mixed-mode cooling, Build. Environ. 71 (2014) 233–244. doi:10.1016/j.buildenv.2013.09.005.
[27] S. Lestinen, S. Kilpeläinen, R. Kosonen, J. Jokisalo, H. Koskela, Experimental study on airflow characteristics with asymmetrical heat load distribution and low-momentum diffuse ceiling ventilation, Build. Environ. 134 (2018) 168–180. doi:10.1016/j.buildenv.2018.02.029.
[28] S. Lestinen, S. Kilpeläinen, R. Kosonen, J. Jokisalo, H. Koskela, A. Melikov, Flow characteristics in occupied zone – An experimental study with symmetrically located thermal plumes and low-momentum diffuse ceiling air distribution, Build. Environ. 128 (2018) 77–88. doi:10.1016/j.buildenv.2017.11.020.
[29] C.A. Hviid, S. Svendsen, Experimental study of perforated suspended ceilings as diffuse ventilation air inlets, Energy Build. 56 (2013) 160–168.

doi:10.1016/j.enbuild.2012.09.010.
[30] D. Zukowska, M. Wolsing, M. Grysbæk, C. Anker, Field Study of Diffuse Ceiling Ventilation Performance in a Landscape Office, in: APA, 2016. https://orbit.dtu.dk/en/publications/field-study-of-diffuse-ceiling-ventilation-performance-in-a-lands (accessed October 30, 2020).
[31] T. Yu, P. Heiselberg, B. Lei, M. Pomianowski, C. Zhang, A novel system solution for cooling and ventilation in office buildings: A review of applied technologies and a case study, Energy Build. 90 (2015) 142–155. doi:10.1016/j.enbuild.2014.12.057.
[32] S. Rahnama, P. Sadeghian, P.V. Nielsen, C. Zhang, S. Sadrizadeh, A. Afshari, Cooling capacity of diffuse ceiling ventilation system and the impact of heat load and diffuse panel distribution, Build. Environ. 185 (2020) 107290. doi:10.1016/j.buildenv.2020.107290.
[33] C. Zhang, T. Yu, P. Heiselberg, M. Pominaowski, P. Nielsen, Diffuse Ceiling Ventilation – Design Guide, 2016. https://vbn.aau.dk/ws/portalfiles/portal/243057526/Diffuse_ceiling_ventilation_Design_guide.pdf (accessed June 5, 2019).
[34] C.A. Hviid, S. Petersen, Integrated ventilation and night cooling in classrooms with diffuse ceiling ventilation, in: 11Th Ökosan, 2011. https://orbit.dtu.dk/en/publications/integrated-ventilation-and-night-cooling-in-classrooms-with-diffu (accessed October 30, 2020).
[35] Dansk Standard, J. Rose, S. Aggerholm, L. Olsen, H.M. Tommerup, C. Rudbeck, Ds 418, Beregning af bygningers varmetab, (2011).
[36] C.A. Hviid, J. Lessing, Experimental study of the heat transfers and passive cooling potential of a ventilated plenum designed for uniform air distribution, in: 12th REHVA World Congr. CLIMA 2016, 2016. https://orbit.dtu.dk/en/publications/experimental-study-of-the-heat-transfers-and-passive-cooling-pote (accessed April 12, 2020).
[37] C. Zhang, P.K. Heiselberg, Q. Chen, M. Pomianowski, Numerical analysis of diffuse ceiling ventilation and its integration with a radiant ceiling system, Build. Simul. 10 (2017) 203–218. doi:10.1007/s12273-016-0318-z.
[38] ISO 8990-1996: Thermal insulation — Determination of steady-state thermal transmission properties — Calibrated and guarded hot box, International Standard, (1996). https://www.iso.org/standard/16519.html.
[39] S. Leenknegt, R. Wagemakers, W. Bosschaerts, D. Saelens, Improving the modelling of surface convection during natural night ventilation in building energy simulation models,

Proc. Build. Simul. 2011 12th Conf. Int. Build. Perform. Simul. Assoc. (2011) 2233–2240. https://limo.libis.be/primo-explore/fulldisplay?docid=LIRIAS1565328&context=L&vid=Lirias&search_scope=Lirias&tab=default_tab&lang=en_US&fromSitemap=1 (accessed September 26, 2020).

[40] EN ISO 13786, Thermal performance of building components – Dynamic thermal characteristics – Calculation methods, (2017). https://webshop.ds.dk/Default.aspx?ID=219&GroupID=91.120.10&ProductID=M289824.

[41] About FTMU Lindab.dk, (n.d.). http://www.lindab.com/dk/pro/products/Pages/FTMU.aspx (accessed July 25, 2020).

[42] J. Le Dreau, P. Heiselberg, R.L. Jensen, Experimental data from a full-scale facility investigating radiant and convective terminals: Uncertainty and sensitivity analysis, Description of the experimental data, Department of Civil Engineering, Aalborg University, 2014. http://vbn.aau.dk/en/publications/experimental-data-from-a-fullscale-facility-investigating-radiant-and-convective-terminals(1ce46b33-cfa8-4979-b112-cd9ab487f9c7).html (accessed October 22, 2020).

[43] O. Kalyanova, F. Zanghirella, P. Heiselberg, M. Perino, R. Jensen, Measuring air temperature in glazed ventilated façades in the presence of direct solar irradiation, 2007. https://vbn.aau.dk/en/publications/measuring-air-temperature-in-glazed-ventilated-facades-in-the-pre (accessed April 5, 2020).

[44] M.H. Kristensen, J.S. Jensen, R.L. Jensen, Air Temperature Measurements Using Dantec Draught Probes, Department of Civil Engineering, Aalborg University, 2015. https://vbn.aau.dk/en/publications/air-temperature-measurements-using-dantec-draught-probes (accessed July 25, 2020).

[45] Thermo Tracer TH9100MR/WR, (n.d.). https://www.infrared.avio.co.jp/en/products/ir-thermo/lineup/th9100mr-wr/index.html (accessed November 18, 2020).

[46] N. Artmann, R. Vonbank, R.L. Jensen, Temperature measurements using type K thermocouples and the Fluke Helios Plus 2287A data logger thermocouples and the Fluke Helios Plus, 2008.

[47] R.L. Jensen, O.K. Larsen, C.-E. Hyldgård, On the Use of Hot-Sphere Anemometers in a Highly Transient Flow in a Double-Skin Facade, Int. Conf. Air Distrib. Rooms, Roomvent. (2007) 13–15. https://vbn.aau.dk/en/publications/on-the-use-of-hot-sphere-anemometers-in-a-highly-transient-flow-i (accessed July 22, 2020).

[48] G.D. Smith, Numerical solution of partial differential equations: finite difference

methods, Oxford university press, 1985. https://anujitspenjoymath.files.wordpress.com/2019/02/g.-d.-smith-numerical-solution-of-partial-differential-equations_-finite-difference-methods.pdf.
[49] A.J. Chapman, Fundamentals of heat transfer, Macmillan, 1987.
[50] J.R. Ehlert, T.F. Smith, View factors for perpendicular and parallel rectangular plates, J. Thermophys. Heat Transf. 7 (1993) 173–175. doi:10.2514/3.11587.
[51] G. Walton, Calculation of obstructed view factors by adaptive integration, Gaithersburg, MD, 2002. doi:10.6028/NIST.IR.6925.
[52] W. Tian, Y. Heo, P. de Wilde, Z. Li, D. Yan, C.S. Park, X. Feng, G. Augenbroe, A review of uncertainty analysis in building energy assessment, Renew. Sustain. Energy Rev. 93 (2018) 285–301. doi:10.1016/j.rser.2018.05.029.
[53] A. Bejan, Convection heat transfer, John wiley & sons, 2013. https://ebookcentral.proquest.com/lib/aalborguniv-ebooks/detail.action?docID=1161535&pq-origsite=primo.
[54] D.E. Fisher, C.O. Pedersen, Convective heat transfer in building energy and thermal load calculations, ASHRAE Trans. 103 (1997) 137–148. https://citeseerx.ist.psu.edu/viewdoc/download?doi=10.1.1.616.9820&rep=rep1&type=pdf.
[55] D.E. Fisher, An experimental investigation of mixed convection heat transfer in a rectangular enclosure, University of Illinois at Urbana-Champaign, 1995. https://www.ideals.illinois.edu/handle/2142/22513.
[56] S. Petersen, N.U. Christensen, C. Heinsen, A.S. Hansen, Investigation of the displacement effect of a diffuse ceiling ventilation system, Energy Build. 85 (2014) 265–274. doi:10.1016/j.enbuild.2014.09.041.
[57] A. Novoselac, B.J. Burley, J. Srebric, Development of new and validation of existing convection correlations for rooms with displacement ventilation systems, Energy Build. 38 (2006) 163–173. doi:10.1016/j.enbuild.2005.04.005.
[58] I. Beausoleil-Morrison, The adaptive simulation of convective heat transfer at internal building surfaces, Build. Environ. 37 (2002) 791–806. doi:10.1016/S0360-1323(02)00042-2.
[59] Mathworks®, Curve Fitting Toolbox™: User's Guide (R2019b), 2019. https://www.mathworks.com/help/curvefit/.
[60] N. Artmann, H. Manz, P. Heiselberg, Climatic potential for passive cooling of buildings by night-time ventilation in Europe, Appl. Energy. 84 (2007) 187–201.

1 doi:10.1016/j.apenergy.2006.05.004.

2